Transformation of protodolomite to dolomite proceeds under dry-heating conditions

Weili Zheng[1, 2], Deng Liu[1, 2, *], Shanshan Yang[2], Qigao Fan[2], Dominic Papineau[1, 3, 4, 5], Hongmei Wang[1, 2], Xuan Qiu[1], Biao Chang[1], and Zhenbing She[1]

[1]State Key Laboratory of Biogeology and Environmental Geology, China University of Geosciences, Wuhan 430074, China

[2]School of Environmental Studies, China University of Geosciences, Wuhan 430074, China

[3]London Centre for nanotechnology, University College London, 17-19 Gordon Street, London, UK

[4]Department of Earth Sciences, University College London, London, UK

[5]Center for Planetary Sciences, University College London and Birkbeck College London, London, UK

Corresponding author: Deng Liu (liudeng@cug.edu.cn)

Accepted in *Earth and Planetary Science Letters*

October 02, 2021

Please cite as: Zheng, W., Liu, D., Yang, S., Fan, Q., Papineau, D., Wang, H., Qiu, X., Chang, B., and She, Z. (2021) Transformation of microbially-induced protodolomite to dolomite proceeds under dry-heating conditions. Earth and Planetary Science Letters 576, 1-10. DOI: 10.1016/j.epsl.2021.117249

ABSTRACT

The genesis of sedimentary dolomite remains an unresolved issue. Protodolomite has been considered as a metastable precursor for some sedimentary dolomites. Through laboratory experiments, much has been learnt about the transformation of protodolomite into dolomite under hydrothermal conditions mimicking those in open diagenetic systems. However, it is still unclear whether such mineral transformation could proceed in closed diagenetic systems, in which the supply of externally-derived fluids is often limited. Here through dry-heating experiments we demonstrated that low-temperature protodolomite converts into dolomite in the absence of external fluid. The starting materials for the recrystallization reactions included two types of protodolomite: biotic protodolomite and its abiotic counterpart. Biotic protodolomite was synthesized by means of a halophilic bacterium at 30 °C. Since the synthesis of abiotic protodolomite normally requires higher temperatures than biotic ones, the abiotic protodolomite samples used herein were prepared at 60 °C and 100 °C. These protodolomites were spherical in shape and composed of nano-globular subunits. Our protodolomite samples contained considerable structural water in the range of 1.4-7 wt%. The water content of protodolomites was linearly correlated with their synthesis temperature, that is, biotic protodolomite had a higher amount of water than its abiotic counterparts. The protodolomite samples were then dry-annealed at temperatures of 100 to 300 °C for two months. The results indicated that the rate of protodolomite-to-dolomite transformation was higher in the reactors using biotic protodolomite than those using abiotic protodolomites. This conversion was likely triggered by the

dehydration of structural water within protodolomite. The resulting dolomite mostly retained spherical morphology, whereas its nanosized subunits tended to become rhombohedral. Calcite neoformation was also found to accompany the dolomite formation. Our findings suggest that structural water within protodolomite is an overlooked internal fluid and it might have an impact on the genesis of sedimentary dolomite during burial diagenesis.

Keywords: dolomite problem, microbially-induced protodolomite, protodolomite-to-dolomite transformation, dry-heating experiment, structural water

1. Introduction

The origin of dolomite [$CaMg(CO_3)_2$] has been a persistent enigma in Earth science (i.e., the "dolomite problem") (Arvidson and Mackenzie, 1999; Warren, 2000; Gregg et al., 2015). The so-called "dolomite problem" is generated by two observations. First, dolomite is abundant in ancient carbonate platforms, but rare in young sediments. Second, dolomite is notoriously difficult to precipitate experimentally at ambient temperatures and pressures (Land, 1998; Arvidson and Mackenzie, 1999; McKenzie and Vasconcelos, 2009).

Although sedimentary dolomites might have multiple origins (McKenzie and Vasconcelos, 2009; Kaczmarek and Thornton, 2017; Petrash et al., 2017; Liu et al., 2019a; Chang et al., 2020), the majority of them have been thought to be a diagenetic replacement of carbonate precursors (Kaczmarek and Thornton, 2017). Hydrothermal

synthesis experiments have demonstrated that protodolomite (also called "disordered dolomite" or sometimes "very high-Mg calcite") is a common metastable precursor for dolomite (e.g., Graf and Goldsmith, 1956; Sibley et al., 1994; Kaczmarek and Sibley, 2011; Rodriguez-Blanco et al., 2015; Kaczmarek and Thornton, 2017). According to the definition of Graf and Goldsmith (1956), protodolomite is a Ca-Mg carbonate that has a dolomite-like composition (> 36 mol% $MgCO_3$) but possesses Ca-Mg disordering of the lattice structure.

Protodolomite has both biotic and abiotic origins (Zhang et al., 2012, 2015; Liu et al., 2019a, b). However, due to the strong solvation shell of Mg^{2+} ions in solution, direct synthesis of abiotic protodolomite at Earth surface temperatures (< 60 °C) remains a challenge. In the past 25 years, a greater attention has been devoted to the catalytic effect of microorganisms on the formation of (proto-)dolomite at ambient temperature (~ 25 °C) (e.g., Vasconcelos et al., 1995; Roberts et al., 2004; Sánchez-Román et al., 2008, 2009; Bontognali et al., 2014; Zhang et al., 2015; Qiu et al., 2017; Daye et al., 2019; Huang et al., 2019; Liu et al., 2019b). It is worthwhile to note, in most of aforementioned cases, that protodolomite rather than dolomite is the biomineralization product (Zhang et al., 2012; Gregg et al., 2015; Huang et al., 2019; Liu et al., 2019b). Because protodolomite is considered a dolomite precursor, a revised microbial dolomite model was proposed to interpret the occurrence of dolomite within Holocene and pre-Holocene microbial mats (Fan et al., 2021). In this model, microbial activities create oversaturated conditions to permit the onset of the protodolomite precipitation and the chemical components of microbial cells can diminish the Mg-hydration effect (Zhang

et al., 2015; Qiu et al., 2017; Huang et al., 2019). Diagenetic experiments show that protodolomite can be converted into dolomite in the presence of brine fluids (Malone et al., 1996; Schmidt et al., 2005). These experiments were performed with high fluid:solid ratio and thus are thought to simulate the process of (proto-)dolomite recrystallization in open diagenetic systems, in which large amounts of externally-derived fluids can be transported into the system and then trigger protodolomite dissolution and subsequent dolomite precipitation.

In closed diagenetic or metamorphic environments, the supply of external fluids is limited (Bjørlykke and Jahren, 2012). Although closed geochemical systems are typically related to deep burial, there is recent evidence showing sediments can also evolve in a relatively closed diagenetic system during early diagenesis (e.g., Zwicker et al., 2018; Liu et al., 2020). It has been reported that biogenic Mg-calcites (e.g., skeletons of invertebrates) can undergo recrystallization even in the absence of an aqueous phase (Gaffey et al., 1991; Dickson, 2001; Lloyd et al., 2018). However, it is not yet clear whether protodolomite could transform into dolomite in a closed diagenetic system. To address this question, we conducted dry-heating experiments to determine how protodolomite evolves when it is subjected to heating spanning conditions from diagenesis to low-grade metamorphism (100-300 °C).

2. Materials and methods

2.1. Preparation of biotic and abiotic protodolomites

Both biotic and abiotic protodolomites were prepared as the starting materials for dry-heating experiments. Our recent work has shown that several halophilic bacteria isolated from a Chinese saline lake (Lake Jibuhulangtu Nuur, Inner Mongolia) are capable of mediating the formation of low-temperature protodolomite and other carbonate minerals (Liu et al., 2019b). Among them, *Halomonas* sp. strain JBHLT-1 has the ability to synthesize highly pure protodolomite (Liu et al., 2019b). As such, this strain was selected for synthesizing biotic protodolomite. Strain JBHLT-1 was aerobically cultivated in glass flasks containing a saline medium as described by Liu et al. (2019b). In brief, this medium consisted of (per liter) 31.82 g NaCl, 3.71 g $MgCl_2$, 0.25 g $CaCl_2$, 16.69 g Na_2SO_4, 0.04 g $NaHCO_3$, 0.04 g Na_2CO_3, 0.06 g KCl, 0.5 g bacto peptone, and 2 g yeast extract. The pH of this medium was adjusted to 9.0 by adding 0.5 M NaOH as needed. After incubated at 30 °C for 9 days, abundant white precipitates (later verified as protodolomite) visually deposited on the bottom of the flasks. The precipitated crystals were collected by centrifugation for 10 min at 8000×g. To remove organic debris and microbial cells, the resulting protodolomite was extensively washed using a detergent solution containing 5% sodium dodecyl sulfate (SDS) and 5% Triton X-100, following the method described previously (Liu et al., 2019b).

Abiotic protodolomite was synthesized by sol-gel and hydrothermal methods (Malone et al., 1996). In brief, 100 mL 1 M $CaCl_2$ was added slowly into 100 mL 1 M $MgSO_4$ with vigorous stirring. Then, 200 mL 1 M $NaCO_3$ was rapidly added into the mixture. The resulting sol-gel solution was heated at 60 °C or 100 °C for 2 days to produce protodolomite. The abiotic protodolomite precipitates were collected by

centrifugation, repeatedly rinsed with doubly distilled water (ddH_2O), and dried in an oven at 60 °C.

2.2. Preparation of abiotic dolomite standard

Abiotic dolomite was prepared as a standard to probe the structural differences between protodolomite and dolomite. This abiotic phase was synthesized following a reported protocol (Rodriguez-Blanco et al., 2015). Briefly, 100 mL of 1 M $CaCl_2$ was added into 100 mL of 1 M $MgCl_2$ solution with vigorous stirring. Then, this Ca-Mg solution was rapidly mixed with an equal volume of 1 M Na_2CO_3, leading to the formation of cloudy colloidal suspensions. The colloidal suspension was added in an apparatus of Teflon-lined hydrothermal bomb. The bomb was immediately placed into an oven and heated at 250 °C for 3 days. The resulting dolomite materials were harvested by centrifugation (8000×g, 10 min), rinsed with ddH_2O, and dried at 60 °C.

2.3. Dry-heating of biotic and abiotic protodolomites

0.5 g aliquots of pre-dried biotic or abiotic protodolomite were added into clean quartz tubes, and the tubes were filled with ultra-pure nitrogen gas and then sealed under vacuum (10^{-3} Torr). Afterwards, these tubes were heated in a muffle furnace at temperatures in the range of 100 °C-300 °C for two months and then quenched to room temperature. The annealed samples were carefully collected for mineralogical analyses.

2.4. Mineralogical analyses

The unannealed and two-month annealed protodolomites, as well as abiotic dolomite standard, were examined by multiple mineralogical techniques, including X-ray diffraction (XRD), Raman spectroscopy, Fourier transformation infrared

spectroscopy (FT-IR), and thermogravimetric-mass spectrometric analysis (TGA-MS). In general, crystal powders were X-rayed using Cu Kα radiation on a Bruker D8 Advance diffractometer from 15 to 55° 2θ with a step size of 0.02° per second. The stoichiometry of (proto-)dolomites (mol%) was calculated from the position of the (104) peak (Bischoff et al., 1983). Raman spectra were collected with a 514 nm laser using a Renishaw RM-1000 spectrometer in the range of 100-2000 cm^{-1}. FT-IR spectra were recorded in the region of 450-4000 cm^{-1} using a Perkin-Elmer 2000 Spectrometer. A TGA instrument (TGA-2050, TA instruments) coupled with a mass spectrometer (Glarus-500, Perkin-Elmer) was employed to investigate the thermal properties of the protodolomite, which was heated from 30°C to 850°C under a N_2 atmosphere.

The changes in morphological and crystallographic properties of (proto-)dolomite before and after heating were determined by scanning and transmission electron microscopy (SEM and TEM), atomic force microscopy (AFM), micro-Raman spectroscopy, and optical microscopy. Prior to SEM observations, crystal samples were mounted onto SEM stubs with double-sided sticky C-tape and sputter-coated with Platinum. SEM images were obtained in the secondary electron mode using a Hitachi SU-8010 SEM operated at 5-10 kV. Focused ion beam (FIB) milling was employed for TEM specimen preparation. FIB milling was performed using a Zeiss Crossbeam XB 540 microscope with FIB system. The finished sections were placed on carbon-coated TEM copper grids. The TEM analyses were carried out using a JEOL-2100F TEM operating at 200 kV. The chemical compositions of (proto-)dolomites were quantitatively analyzed with an energy-dispersive X-ray spectroscopy (EDS; Bruker

Quantax 200) equipped on the TEM. AFM topographical imaging was performed on a Bruker Multimode AFM system working in contact mode at ambient conditions. The cantilever of the AFM probe was a standard Si_3N_4 microlever with free resonance frequencies around 200 kHz. The images were recorded at a scan rate of 0.5-2 Hz. The micro-Raman measurements were accomplished using Alpha confocal Raman microscope system (Witec, Germany) equipped with a 532-nm excitation laser and a 100× objective. The acquisition time was 30 s per position. The resulting Raman data were analyzed using Witec Project 5.1 plus software.

3. Results

3.1. Mineralogical differences between protodolomite and dolomite

Both unannealed biotic and abiotic protodolomites had similar patterns of XRD and FT-IR to abiotic dolomite standard that was hydrothermally synthesized at 250 °C (Fig. 1a, b). However, differences in crystal structure could be observed between protodolomite and dolomite. Most notably, in the comparison between the abiotic dolomite standard and the protodolomite that was produced either biotically or abiotically, all peaks of the latter were broader (Fig. 1a, b). A similar conclusion can also be drawn from broader Raman peaks (Fig. S1). In addition, the superlattice XRD reflections [e.g., (101), (015) and (021)], characteristics of ordered dolomite, were absent in biotic and abiotic protodolomites (Fig. 1a), which indicates that the latter phases had disordered cations. According to their $d(104)$ values, the $MgCO_3$ content was 46.38 mol% (d_{104}=2.906 Å) for biotic protodolomite (30 °C), 48.92 mol%

198 (d_{104}=2.899 Å) for 60 °C synthetic abiotic protodolomite, and 49.66 mol% (d_{104}=2.897
199 Å) for 100 °C synthetic abiotic sample, respectively. It is relevant to note that OH bands
200 (ν1+ν3; 3000-3800 cm^{-1}) occurred in two types of protodolomite, but not in the abiotic
201 dolomite standard (Fig. 1b), suggesting that both biotic and abiotic protodolomites were
202 in a hydrous state. Noticeably, the OH signal in biotic protodolomite was significantly
203 stronger than that in abiotic protodolomite (either 60 °C or 100 °C) (Fig. 1b). The
204 hydrous nature of protodolomite was further confirmed by TGA-MS measurements.
205 The TGA-MS data showed distinct responses for protodolomite and dolomite (Fig. 1c).
206 Specifically, a single weight loss step of 49.4% between 380 and 780 °C was observed
207 in the TGA curve of the abiotic dolomite standard. By contrast, three significant weight
208 loss events occurred when biotic or abiotic protodolomite was subjected to thermal
209 decomposition (Fig. 1c). The first loss event at lower than 400 °C might be due to the
210 vaporization of protodolomite-bound water, whereas the two others can be interpreted
211 as a result of mineral decarbonation (Liu et al., 2019b). Moreover, the presence of water
212 vapor within the heating range of 100-350 °C, corresponds to 7% of biotic
213 protodolomite mass, 4.8 wt% of 60 °C synthetic abiotic protodolomite, and 1.4 wt% of
214 100 °C synthesis (Fig. 1c). Furthermore, our TGA-MS data are consistent with
215 aforementioned FT-IR results showing that biotic protodolomite displayed a higher
216 amount of mineral-bound water than its abiotic counterparts. There was a previous
217 study reporting that a hydrous protodolomite that was abiotically synthesized at 81 °C
218 had a water content of ~2.5 wt% (Kelleher and Redfern, 2002). Interestingly, our new

219 results in combination with this published data showed that the water content of
220 protodolomites is linearly correlated with their synthesis temperature (Fig. 1d).

221 **3.2. Transformation of protodolomite by dry heating**

222 Significant changes in crystal structure and mineralogy can be observed when two
223 types of protodolomite were subjected to heating treatments (Figs. 2 and 3). Specifically
224 for annealed biotic protodolomite, as revealed by FT-IR data, the intensity of OH bands
225 gradually decreased from 150 to 300 °C, while other bands became sharper (Fig. 2a).
226 The thermal treatment also led to sharper XRD peaks (Fig. 2b). Such alteration could
227 be demonstrated by the decline in the values of full width at half maximum (FWHM)
228 of the (104) peak (Fig. 2c). More importantly, the superlattice reflections emerged when
229 the biotic protodolomite was heated at 200 °C, and their signals were more intense at
230 300 °C (Fig. 2b), showing that biotic protodolomite can transform into dolomite under
231 dry-heating conditions. Furthermore, the biotic protodolomite samples heated either at
232 200 °C or at 300 °C had a more stoichiometric composition (i.e., closer to 50 mol%
233 $MgCO_3$) than the ones treated at lower temperatures (Fig. 2d). Similar to that of biotic
234 protodolomite, the XRD reflections of abiotic protodolomite that was originally
235 synthesized at 60 °C also became sharper after dry-heating treatments (Fig. 3a, b).
236 However, only the (015) superlattice reflection was observed in the abiotic sample
237 synthesized at 60 °C upon heating at 200 °C (Fig. 3a), indicating that the crystals were
238 weakly ordered. All the superlattice reflections became visible for this sample when the
239 annealing temperature was increased to 300 °C. In contrast, superlattice peaks were
240 absent in the 100 °C-synthesized samples after thermal treatments (Fig. 3c), and the

241 FWHM values of the (104) peak for these samples declined only slightly (Fig. 3d).
242 Short XRD scans in the 2θ range of 30-38º clearly showed the distinct transformation
243 rates among protodolomites (as indicated by the intensity of (015) peak) (Fig. 4). The
244 order of protodolomite-to-dolomite transformation rate was as follows: biotic
245 protodolomite > 60 °C-synthesized abiotic protodolomite >100 °C-synthesized abiotic
246 protodolomite.

247 In addition to dolomite, traces of low-Mg calcite with $MgCO_3$ contents of ca. 5.25
248 mol% (d_{104}=3.019 Å) were also detected in the annealed biotic protodolomite samples
249 either heated at 200 °C or 300 °C and in the 60 °C-synthesized abiotic protodolomite
250 sample heated at 300 °C (Figs. 2b, 3a and Fig. S2). The biotic protodolomite sample
251 heated at 200 °C was selected to further observe the spatial association between calcite
252 and dolomite by using micro-Raman, SEM-EDS and TEM (Fig. 5). The micro-Raman
253 results indicated that calcite (characteristic ν1 band at 1085 cm^{-1}) occurred along the
254 grain boundaries of dolomite (characteristic ν1 band at 1095 cm^{-1}) (Fig. 5a, b). The low
255 Mg content can be employed as a criterion to identify calcite in the annealed samples.
256 As revealed by SEM image, Ca/Mg elemental mappings and EDS spot analyses, some
257 micro-domains between dolomite spheroids displayed a significantly weaker Mg signal
258 (Fig. 5c-e), and thus were identified as calcite. The co-occurrence of calcite was also
259 confirmed by TEM observations (Fig. 5g). The lattice-resolved image showed the
260 dominant spacing of 2.49 Å, which corresponds to the (110) plane of calcite. Moreover,
261 the ring-shaped pattern of selected area electron diffraction (SAED) demonstrated that
262 calcite crystals had a random orientation (Fig. 5g).

3.3. Morphology and crystal structure of (proto-)dolomites before and after annealing

SEM images showed that both unannealed biotic and abiotic protodolomites occurred as microspheroidal aggregates (Fig. 6a and Fig. S3). Higher magnification views further revealed that microspheroidal protodolomite was composed of densely-packed nanoglobules, with a mean size of 28 nm for biotic protodolomite (Fig. 6b, c), 66 nm for the 60 °C-synthesized abiotic protodolomite (Fig. S3b), and 73 nm for the 100 °C synthesis (Fig. S3d), respectively. After heating at 200 °C or 300 °C, the newly-formed dolomite generated from recrystallization of low-temperature protodolomite (30 °C or 60 °C) retained the spheroidal morphology but exhibited a coarser texture with larger, euhedral nanoscopic grains (Fig. 6d-I and Fig. S3e-f).

According to AFM data, the average size of dolomite crystals that were generated from annealed biotic protodolomite was ca. 103 nm at 200 °C and 195 nm at 300 °C, respectively (Fig. 6f, i). In addition, thermal treatment resulted in the formation of irregular cavities on the surface of spheroidal dolomite (Fig. 6e, h).

FIB-cross sections of unannealed biotic protodolomite and from experiments annealed at 200 °C were selected as representative examples for TEM observations (Fig. 7). TEM images showed that nanoglobules of unannealed biotic protodolomite were randomly packed in high density (Fig. 7a, b). The corresponding EDS data revealed that the Ca content of protodolomite was slightly higher than its Mg content (Fig. 7b). The characteristic lattice fringe spacing of 2.907 Å (Fig. 7c) corresponds to the (104) plane of protodolomite, consistent with the XRD results described above (Fig. 2a). The

285 cation-disordered nature of protodolomite was also confirmed by the fast Fourier
286 transform (FFT) pattern, as (003) and other superlattice reflections were invisible (Fig.
287 7c). The FIB section of the sample annealed at 200 °C clearly showed widespread cavity
288 structures as nanoscopic pores between euhedral crystals (Fig. 7d, e). These euhedral
289 dolomite grains contained nearly equal amounts of Mg and Ca and their habit had a
290 notable near-rhombohedral morphology (Fig. 7e). This stands in contrast with the
291 significantly smaller spherical to amorphous morphology of crystallites observed in
292 unannealed biotic protodolomite (Fig. 7b). Observed lattice fringes of 2.670 Å are in
293 agreement with the (006) plane of dolomite and the corresponding FFT pattern clearly
294 also showed the occurrence of (003) reflection, which is an indicator of cation ordering
295 (Fig. 7f).
296
297 **4. Discussion**
298 **4.1. The hydrous nature of protodolomite**
299 Besides the lack of superlattice reflections, as shown herein, the XRD peaks of
300 unannealed protodolomite that was synthesized either biotically or abiotically were
301 rather broader than those of dolomite (Fig. 1a). It is generally thought that a broad XRD
302 peak is indicative of a small particle size (Kurlov and Gusev, 2007). This conclusion is
303 independently supported by the presence of nanoscopic amorphous crystallites in the
304 unaltered protodolomites demonstrated by our electron and atomic force microscopic
305 observations (Figs. 6, 7 and Fig. S3).

306 There is an alternative view that structurally-coordinated water could also account
307 for the XRD peak broadening (Kelleher and Redfern, 2002; Holmboe et al., 2012).
308 Unlike abiotic dolomite which was nearly anhydrous, our FT-IR and TGA-MS data
309 collectively demonstrated that protodolomite contained water molecules to different
310 extents (Fig. 1b-d). Coordinated water is commonly found in low-temperature minerals,
311 such as clay minerals (Johnston, 2018). However, in many cases, the water molecules
312 are adsorbed on mineral surfaces rather than structurally-coordinated (Wang et al.,
313 2006). In fact, the mass-loss observed in TGA curves below 150 °C is typically
314 attributed to dehydration of water adsorbed on mineral surfaces (e.g., Li et al., 2019).
315 Our TGA-MS results indicated that the generation of major water vapor during the
316 thermal decomposition of protodolomite occurred at temperatures above 150 °C (Fig.
317 6d), and thus were not adsorbed on mineral grain surfaces. Instead, this finding suggests
318 that most water molecules were bonded in the structure of protodolomite.

319 In fact, the existence of structural water is a common feature of low-temperature
320 magnesium carbonates, such as hydromagnesite [$Mg_5(CO_3)_4(OH)_2{\cdot}4H_2O$] and
321 nesquehonite ($MgCO_3{\cdot}3H_2O$) (Xu et al., 2013). Some natural or synthetic Ca-Mg
322 carbonates have been demonstrated to be hydrous (Kelleher and Redfern, 2002;
323 Schmidt et al., 2005). For example, Kelleher and Redfern (2002) conducted abiotic
324 synthesis experiments and reported a protodolomite phase which had a water content
325 of ca. 2.5 wt%. Such hydrous low-temperature Mg-bearing carbonates, including
326 protodolomite, might be attributed to the Mg-hydration effect. Among alkaline-earth
327 cations, Mg^{2+} has one of the smallest ionic radius (after Be^{2+}) but it also has the largest

hydrated radius (Lippmann, 1973; Xu et al., 2013). As a result, when Mg^{2+} cations are dissolved into solution, it will tend to form Mg-H_2O complexes (i.e., $[Mg(H_2O)_6]^{2+}$), which have been demonstrated to hinder the binding of Mg^{2+} to carbonate anions (Shen et al., 2015).

Typically, the tight hydration of Mg^{2+} in aqueous solution can be gradually weakened with increasing temperatures (Xu et al., 2013), which can explain the fact that abiotic protodolomite and ordered dolomite can be successfully synthesized in our hydrothermal systems at 60 °C and 250 °C, respectively. The presence of structural water in abiotic protodolomite indicates that the synthesis temperature used was not high enough to fully dehydrate Mg^{2+} ions during the growth of protodolomite. However, a growing body of evidence reports that microbial surface-associated carboxyl groups are effective in disturbing the Mg-H_2O association even at temperatures lower than 60 °C (Kenward et al., 2013; Roberts et al., 2013; Qiu et al., 2017; Huang et al., 2019; Liu et al., 2019b; Paulo et al., 2020). A metal-chelation model has been proposed to interpret the catalytic role of carboxyl groups (Roberts et al., 2013). In general, carboxyl group can bind Mg-H_2O complex via electrostatic attraction, leading to formation of Mg-H_2O-carboxyl complexes (i.e., $[Mg(H_2O)_5(R\text{-}COO)]^{+}$). This newly-formed Mg-$H_2O$-carboxyl complex requires much lower energy for carbonation (Roberts et al., 2013). However, a recent study using atomistic simulations revealed that the dehydration of water from Mg^{2+} remains incomplete even with the aid of microorganisms (Shen et al., 2015). According to this view, upon microbial carbonation, water molecules would be trapped within the lattice of biotic protodolomite or other

Mg-bearing carbonates. Moreover, our results showed that more structural water existed in biotic protodolomite (formed at 30 °C) as compared to its abiotic counterparts (formed at 60 °C and 100 °C). This discrepancy is attributed to the different synthesis temperatures that were employed for producing these two types of protodolomite, that is, higher synthesis temperature can result in lower content of mineral-bound water (Fig. 1d).

4.2. The mechanism of protodolomite-to-dolomite transformation under dry-heating conditions

In the present study, we showed that formation of dolomite can be achieved by thermal transformation of low-temperature protodolomite (i.e., synthesized below 60 °C) in the absence of external fluids. Such thermal transformation implies that the initial dehydration was followed by a recrystallization during which structurally-bound water was removed while the nanoscopic amorphous solid became a sub-micron crystalline mineral. It is important to note, on the basis of serial FT-IR analyses for progressively heated biotic protodolomite (Fig. 2a), that such transformation was accompanied by the loss of structural water. Furthermore, protodolomite samples having higher water content had a significantly higher transformation rate (Fig. 4). Therefore, it is reasonable to assume that structural water played an important role in protodolomite transformation. As evidenced by TGA-MS, heating of protodolomite released waters, but at a higher temperature than expected. This released water might trigger the dissolution of protodolomite in the same fashion as external fluids. Our microscopic results provided evidence for the dissolution of low-temperature

372 protodolomite, as unannealed protodolomite possessed tightly packed nano-
373 architectures, while cavities were commonly found in the heated samples annealed at
374 or higher than 200 °C (Figs. 5 and 6). Protodolomite dissolution was also indirectly
375 evidenced by the occurrence of neoformed calcite in the heating systems. Compared to
376 dolomite, our protodolomite had higher $CaCO_3$ content (corresponding to lower
377 $MgCO_3$ content). During the dry-heating process, Mg^{2+}, Ca^{2+} and CO_3^{2-} ions can be
378 released from protodolomite into exsolved waters. These ions recombine to form
379 dolomite once the heating temperature can overcome the energy barrier to dolomite
380 crystallization. The excess Ca^{2+} ions attract CO_3^{2-} ions to form calcite.

381 **4.3. Geological implications**

382 The protodolomite microspherulites produced either biotically or abiotically were
383 formed by aggregation of nanoscopic subunits (Fig. 6 and Fig. S3). These subunits were
384 also spherical in shape (Figs. 6b-c). After dry-heating treatment, the spherical subunits
385 of low-temperature protodolomite became cation-ordered as well as larger in size by at
386 least two orders of magnitude and rhombohedral (Fig. 7e). However, the nanoscopic
387 subunit aggregates remained spheroidal and with a similar diameter in the temperature
388 range examined (Fig. 6 and Fig. S3). This observation is in contrast to previous
389 hydrothermal studies showing the disappearance of original spheroidal structures
390 during dolomitization (e.g., Malone et al., 1996). Therefore, our finding suggests that
391 the morphological feature of protodolomite can be preserved in closed diagenetic
392 environments, during the dehydration phase of lithification, and without alteration by
393 external fluids. The globule-shaped morphology and aggregate texture of

(proto-)dolomite were suggested as potential biosignatures to infer past microbial activities (Warthmann et al., 2000). However, essentially no difference was observed in the morphology between biotic protodolomite and its abiotic counterpart before and after thermal treatment. As such, our results demonstrated that morphology alone cannot serve as a hallmark indicative of a biotic origin for sedimentary dolomite.

Our laboratory stimulation experiments indicated that even biotic protodolomite that had the highest amounts of structural water persisted at 150 °C and the protodolomite-to-dolomite transformation was initiated at temperatures above 200 °C in dry-heating systems. This temperature is within the late-diagenetic temperature range, but higher than the experimental temperatures required for hydrothermal dolomitization that can be achieved below 100 °C within two months (e.g., Malone et al., 1996), which indicates that the invoked dry-heating reaction is a relatively slow process. In addition to temperature, it is relevant to note that reaction time is also important in governing the rate of dolomitization (Arvidson and Mackenzie, 1999). It has been well documented that the formation of dolomite at lower temperature requires longer time duration (Usdowski, 1994; Malone et al., 1996; Arvidson and Mackenzie, 1999; Kaczmarek and Thornton, 2017). For instance, Usdowski (1994) reported that hydrothermal replacement of calcite by dolomite could take place between 60 and 90 °C after seven years. A modeling work by Arvidson and Mckenzie (1999) further indicated that crystallization of dolomite at 40 °C requires tens of years. Given the fact that the reaction rate of dry-heating transformation is slower than that of hydrothermal replacement, two-month of heating treatment below 200 °C tested in this study may not

be enough to observe the crystallization of dolomite. Future experiments are now needed using longer duration (such as several decades) to examine whether the dry-heating protodolomite-to-dolomite transformation could occur at lower temperatures which can be related to early diagenesis. Our experiments also indicated that neoformed calcite was observed to accompany the protodolomite-to-dolomite transformation. Calcite has been repeatedly found in dolostones (e.g., Tan and Hudson, 1971; Li et al., 2021). These co-existing calcites were often interpreted as residual precursors during dolomitization (Tan and Hudson, 1971; Li et al., 2021). Based on our present findings, however, they may be a co-product during recrystallization of protodolomite in a closed diagenetic system.

Unlike open diagenetic systems, the sediment pore spaces in closed diagenetic system are completely or partly filled during carbonate cementation, resulting in little exchange of external fluids (Bjørlykke and Jahren, 2012; Luo et al., 2019). However, mineral dissolution and precipitation can still occur in the closed diagenetic system because of the existence of internal fluids (i.e., self-sourced fluids) (Bjørlykke and Jahren, 2012). According to the conventional view, internal fluids are mainly sourced from the original porewater within sediments and the dehydration of clay minerals (Liu et al., 2020). In the present study, we demonstrated that water can be released during protodolomite annealing. Therefore, structural water within low-temperature protodolomite is an alternative type of internal fluids and it can have an impact on mineral alteration in the diagenetic environments.

5. Conclusions

Through experiments, we demonstrated that low-temperature protodolomite can be converted abiotically into dolomite under a dry-heating treatment. The protodolomite samples produced either biotically or abiotically were characterized by a microscopic spheroidal morphology composed of nanoscopic amorphous crystals. These two types of protodolomite contained considerable amounts of structural water as compared with the abiotic dolomite standard, but had approximately equal levels of Ca and Mg. Visible superlattice reflections from abiotic dolomite could be found in the protodolomite samples synthesized at 30 °C or 60 °C on heating at 200 °C or higher, however, they were absent in the annealed sample that was originally synthesized at 100 °C. The loss of structural water was accompanied by the protodolomite-to-dolomite transformation. Our results thus reveal that the protodolomite-to-dolomite transformation can proceed in a closed diagenetic system with protodolomite acting as a source of internal water.

Acknowledgements

We are thankful to Prof. Shucheng Xie, Prof. Genming Luo and Dr. Yangguang Ou for their helpful discussions and/or laboratory assistance. This project was funded by the National Natural Science Foundation of China (Nos. 41772362 and 42072336), the Strategic Priority Research Program of Chinese Academy of Sciences (No. XDB26000000), and the 111 Project (No. BP0820004). The authors also gratefully acknowledge the insightful comments and suggestions made by Prof. Laurence Coogan

(the editor), Prof. Rolf S. Arvidson, and an anonymous reviewer.

References

Arvidson, R.S., Mackenzie, F.T., 1999. The dolomite problem: control of precipitation kinetics by temperature and saturation state. Am J Sci. 299, 257-288.

Bischoff, W.D., Bishop, F.C., Mackenzie, F.T., 1983. Biogenically produced magnesian calcite: inhomogeneities in chemical and physical properties; comparison with synthetic phases. Am. Mineral. 68, 1183-1188.

Bjørlykke, K., Jahren, J., 2012. Open or closed geochemical systems during diagenesis in sedimentary basins: Constraints on mass transfer during diagenesis and the prediction of porosity in sandstone and carbonate reservoirs. AAPG Bull. 96(12), 2193-2214.

Bontognali, T.R.R., McKenzie, J.A., Warthmann, R.J., Vasconcelos, C., 2014. Microbially influenced formation of Mg-calcite and Ca-dolomite in the presence of exopolymeric substances produced by sulphate-reducing bacteria. Terra Nova 26, 72-77.

Chang, B., Li, C., Liu, D., Foster, I., Tripati, A., Lloyd, M.K., Maradiaga, I., Luo, G., An, Z., She, Z., Xie, S., Tong, J., Huang, J., Algeo, T.J., Lyons, T.W., Immenhauser, A., 2020. Massive formation of early diagenetic dolomite in the Ediacaran ocean: Constraints on the “dolomite problem”. Proc. Natl. Acad. Sci. U. S. A. 117, 14005-14014.

Daye, M., Higgins, J., Bosak, T., 2019. Formation of ordered dolomite in anaerobic

photosynthetic biofilms. Geology 47, 509-512.

Dickson, J.A.D., 2001. Tranformation of echinoid Mg calcite skeletons by heating. Geochim. Cosmochim. Acta 55, 1627-1640.

Fan, Q., Liu, D., Papineau, D., Qiu, X., Wang, H., She, Z., Zhao, L., 2021. Precipitation of high Mg-calcite and protodolomite using dead biomass of aerobic halophilic bacteria. J. Earth Sci. in press.

Gaffey, S.J., Kolak, J.J., Bronnimann, C.E., 1991. Effects of drying, heating, annealing, and roasting on carbonate skeletal material, with geochemical and diagenetic implications. Geochim. Cosmochim. Acta 65, 443-454.

Graf, D.L., Goldsmith, J.R., 1956. Some hydrothermal syntheses of dolomite and protodolomite. J. Geol. 64, 173-186.

Gregg, J.M., Bish, D.L., Kaczmarek, S.E., Machel, H.G., 2015. Mineralogy, nucleation and growth of dolomite in the laboratory and sedimentary environment: a review. Sedimentology 62, 1749-1769.

Holmboe, M., Wold, S., Jonsson, M., 2012. Porosity investigation of compacted bentonite using XRD profile modeling. J. Contam. Hydrol. 128, 19-32.

Huang, Y., Yao, Q., Li, H., Wang, F., Zhou, G., Fu, S., 2019. Aerobically incubated bacterial biomass-promoted formation of disordered dolomite and implication for dolomite formation. Chem. Geol. 523, 19-30.

Johnston, C.T., 2018. Clay mineral-water interactions. Schoonheydt, R., Johnston, C.T., Bergaya, F., eds., Surface and Interface chemistry of Clay Minerals, Elsevier, pp. 89-124.

Kaczmarek, S.E., Sibley, D.F., 2011. On the evolution of dolomite stoichiometry and cation order during high-temperature synthesis experiments: An alternative model for the geochemical evolution of natural dolomites. Sediment. Geol. 240, 30-40.

Kaczmarek, S.E., Thornton, B.P., 2017. The effect of temperature on stoichiomety, cation ordering, and reaction rate in high-temperature dolomitization experiments. Chem. Geol. 468, 32-41.

Kelleher, I.J., Redfern, S.A.T., 2002. Hydrous calcium magnesium carbonate, a possible precursor to the formation of sedimentary dolomite. Mol. Simulat. 28, 557-572.

Kenward, P.A., Fowle, D.A., Goldstein, R.H., Ueshima, M., González, L.A., Roberts, J.A., 2013. Ordered low-temperature dolomite mediated by carboxyl-group density of microbial cell walls. AAPG Bull. 97, 2113-2125.

Kurlov, A.S., Gusev, A.I., 2007. Determination of the particle sizes, microstrains, and degree of inhomogeneity in nanostructured materials from X-ray diffraction data. Glass Phys. Chem. 33, 276-282.

Land, L.S., 1998. Failure to precipitate dolomite at 25°C from dilute solution despite 1000-fold oversaturation after 32 years. Aquat. Geochem. 4, 361-368.

Li, H., Yao, Q., Wang, F., Huang, Y., Fu, S., Zhou, G., 2019. Insights into the formation mechanism of vaterite mediated by a deep-sea bacterium *Shewanella piezotolerans* WP3. Geochim. Cosmochim. Acta 256, 35-48.

Li, J., Zhang, H., Cai, Z., Zou, H., Hao, F., Wang, G., Li, P., Zhang, Y., He, J., Fei, W.,

526 2021. Making sense of pore systems and the diagenetic imapcts in the Lower
527 Triassic porous dolostones, northeast Sichuan Basin. J. Petrol. Sci. Eng. 197,
528 107949.
529 Lippmann, F., 1973. Crystal chemistry of sedimentary carbonate minerals, Sedimentary
530 Carbonate Minerals. Springer, pp. 5-96.
531 Liu, D., Xu, Y., Papineau, D., Yu, N., Fan, Q., Qiu, X., Wang, H., 2019a. Experimental
532 evidence for abiotic formation of low-temperature proto-dolomite facilitated by
533 clay minerals. Geochim. Cosmochim. Acta 247, 83-95.
534 Liu, D., Yu, N., Papineau, D., Fan, Q., Wang, H., Qiu, X., She, Z., Luo, G., 2019b. The
535 catalytic role of planktonic aerobic heterotrophic bacteria in protodolomite
536 formation: Results from Lake Jibuhulangtu Nuur, Inner Mogolia, China.
537 Geochim. Cosmochim. Acta 263, 31-49.
538 Liu, M., Xiong, Y., Xiong, C., Liu, Y., Liu, L., Xiao, D., Tan, X., 2020. Evolution of
539 diagenetic system and its controls on the reservoir quality of pre-salt dolostone:
540 The case of the Lower Ordovician Majiagou Formation in the central Ordos
541 Basin, China. Mar. Petrol. Geol. 122, 104674.
542 Lloyd, M.K., Ryb, U., Eiler, J.M., 2018. Experimental calibration of clumped isotope
543 reordering in dolomite. Geochim. Cosmochim. Acta 242, 1-20.
544 Luo, L., Meng, W., Gluyas, J., Tan, X., Gao, X., Feng, M., Kong, X., Shao, H., 2019.
545 Diagenetic characteristics, evolution, controlling factors of diagenetic system
546 and their impacts on reservoir quality in tight deltaic sandstones: Typical
547 example from the Xujiahe Formation in Western Sichuan Foreland Basin, SW

548 China. Mar. Petrol. Geol. 103, 231-254.
549 Malone, M.J., Baker, P.A., Burns, S.J., 1996. Recrystallization of dolomite: An
550 experimental study from 50-200°C. Geochim. Cosmochim. Acta 60, 2189-2207.
551 McKenzie, J.A., Vasconcelos, C., 2009. Dolomite Mountains and the origin of the
552 dolomite rock of which they mainly consist: historical developments and new
553 perspectives. Sedimentology 56, 205-219.
554 Petrash, D.A., Bialik, O.M., Bontognali, T.R.R., Vasconcelos, C., Roberts, J.A.,
555 McKenzie, J.A., Konhauser, K.O., 2017. Microbially catalyzed dolomite
556 formation: From near-surface to burial. Earth-Sci. Rev. 171, 558-582.
557 Qiu, X., Wang, H., Yao, Y., Duan, Y., 2017. High salinity facilitates dolomite
558 precipitation mediated by *Haloferax volcanii* DS52. Earth Planet. Sci. Lett. 472,
559 197-205.
560 Roberts, J.A., Bennett, P.C., González, L.A., Macpherson, G., Milliken, K.L., 2004.
561 Microbial precipitation of dolomite in methanogenic groundwater. Geology 32,
562 277-280.
563 Roberts, J.A., Kenward, P.A., Fowle, D.A., Goldstein, R.H., González, L.A., Moore,
564 D.S., 2013. Surface chemistry allows for abiotic precipitation of dolomite at low
565 temperature. Proc. Natl. Acad. Sci. U. S. A. 110, 14540-14545.
566 Rodriguez-Blanco, J.D., Shaw, S., Benning, L.G., 2015. A route for the direct
567 crystallization of dolomite. Am. Mineral. 100, 1172-1181.
568 Sánchez-Román, M., Vasconcelos, C., Schmid, T., Dittrich, M., McKenzie, J.A., Zenobi,
569 R., Rivadeneyra, M.A., 2008. Aerobic microbial dolomite at the nanometer

570 scale: Implications for the geologic record. Geology 36, 879-882.
571 Sánchez-Román, M., McKenzie, J.A., Wagener, A.D.L.R., Rivadeneyra, M.A.,
572 Vasconcelos, C., 2009. Presence of sulfate does not inhibit low-temperature
573 dolomite precipitation. Earth Planet. Sci. Lett. 285, 131-139.
574 Schmidt, M., Xeflide, S., Botz, R., Mann, S., 2005. Oxygen isotope fractionation during
575 synthesis of CaMg-carbonate and implications for sedimentary dolomite
576 formation. Geochim. Cosmochim. Acta 69(19), 4665-4674.
577 Shen, Z., Szlufarska, I., Brown, P.E., Xu, H., 2015. Inverstigation of the role of
578 polysaccharide in the dolomite growth at low temperature by using atomistic
579 simulations. Langmuir 31(38), 10435-10442.
580 Sibley, D.F., Nordeng, S.H., Borkowski, M.L., 1994. Dolomitization kinetics of
581 hydrothermal bombs and natural settings. J. Sediment. Res. 64(3a), 630-637.
582 Tan, F.C., Hudson, J.D., 1971. Carbon and oxygen isotopic relationships of dolomites
583 and co-existing calcites, Great Estuarine Series (Jurassic), Scotland. Geochim.
584 Cosmochim. Acta 35(8), 755-767.
585 Usdowski, E., 1994. Synthesis of dolomite and geochimical implications. In Purser, B.
586 H., Tucker, M. E., Zenger, D (Editors). Dolomite: A Volume in Honour of
587 Dolomieu, International Association of Sedimentologists Special Publication 21:
588 Blackwell, Oxford, UK. pp.. 345-360.
589 Vasconcelos, C., McKenzie, J.A., Bernasconi, S., Grujic, D., Tiens, A.J., 1995.
590 Microbial mediation as a possible mechanism for natural dolomite formation at
591 low temperatures. Nature 377, 220-222.

592 Wang, J., Kalinichev, A.G., Kirkpatrick, R.J., 2006. Effects of substrate structure and
593 composition on the structure, dynamics, and energetics of water at mineral
594 surfaces: A molecular dynamics modeling study. Geochim. Cosmochim. Acta
595 70(3), 562-582.
596 Warren, J., 2000. Dolomite: occurrence, evolution and economically important
597 associations. Earth-Sci. Rev. 52, 1-81.
598 Warthmann, R., van Lith, Y., Vasconcelos, C., McKenzie, J.A., Karpoff, A.M., 2000.
599 Bacterially induced dolomite precipitation in anoxic culture experiments.
600 Geology 28(12), 1091-1094.
601 Xu, J., Yan, C., Zhang, F., Konishi, H., Xu, H., Teng, H.H., 2013. Testing the cation-
602 hydration effect on the crystallization of Ca-Mg-CO_3 systems. Proc. Natl. Acad.
603 Sci. U. S. A. 110, 17750-17755.
604 Zhang, F., Xu, H., Konishi, H., Shelobolina, E.S., Roden, E., 2012. Polysaccharide-
605 catalyzed nucleation and growth of disordered dolomite: A potential precursor
606 of sedimentary dolomite. Am. Mineral. 97, 556-567.
607 Zhang, F., Xu, H., Shelobolina, E.S., Konishi, H., Converse, B., Shen, Z., Roden, E.E.,
608 2015. The catalytic effect of bound extracellular polymeric substances excreted
609 by anaerobic microorganisms on Ca-Mg carbonate precipitation: Implications
610 for the “dolomite problem”. Am. Mineral. 100, 483-494.
611 Zwicker, J., Smrzka, D., Himmler, T., Monien, P., Gier, P., Goedert, J.L., Peckmann, J.,
612 2018. Rare earth elements as tracers for microbial activity and early diagenesis:
613 A new perspective from carbonate cements of ancient methane-seep deposits.

614 Chem. Geol. 501, 77-85.

615 **Figure caption:**

616 **Figure 1.** Mineralogical comparisons showing the differences between unannealed
617 protodolomites and hydrothermally-synthesized abiotic dolomite standard. (a) XRD
618 patterns with Miller indices with the symbol * denoting superlattice reflections. Note
619 the broader peaks for biotic and abiotic protodolomites in the XRD pattern as well as
620 in the (b) FT-IR spectrum. (c) Comparison of dehydration and decarbonation profiles
621 with increasing temperatures using TGA-MS curves. (d) Linear relationship between
622 water content of protodolomites and their synthesis temperature.

623

624 **Figure 2.** Changes in FT-IR spectra and XRD patterns of biotic protodolomite after
625 heating for two months. Note the peaks become progressively narrow with increasing
626 temperature in (a) FT-IR spectra and (b) XRD patterns. Plots for biotic protodolomite
627 showing the relationship between heating temperature and (c) FWHM of (104) and (d)
628 $MgCO_3$ content calculated from the (104) position.

629

630 **Figure 3.** (a) XRD patterns of 60 °C-synthesized abiotic protodolomite without and
631 with the dry-heating treatment (with the symbol * denoting superlattice reflections) and
632 (b) relationship of FWHM values of (104) peak to heating temperature. (c-d) Changes
633 in XRD patterns of 100 °C-synthesized abiotic sample and FWHM values of (104)
634 reflection as a function of thermal treatment.

635

Figure 4. Short XRD scans showing the distinct transformation rate of biotic and abiotic protodolomites under dry-heating conditions. The black arrows indicate the (015) superlattice peak.

Figure 5. (a-b) Light microscopic photograph and Raman spectra of the heated biotic protodolomite samples at 200 °C; (c) SEM image of annealed samples; (d-e) Ca/Mg elemental mappings of the selected area in panel c. The open circle in panel e highlights the Mg-poor parts of annealed samples; (f) EDS spot analyses showing the occurrence of calcite and dolomite; (g) TEM image, lattice fringes and related SAED of calcite crystals.

Figure 6. SEM and AFM images of unannealed biotic protodolomite (a-c), which always occurred as spheres and of the heated biotic samples at 200 °C (d-f) and at 300 °C (g-i), which mostly retained their sphericity.

Figure 7. FIB and TEM-EDS analyses showing the differences between pristine biotic protodolomite (a-c) and annealed sample at 200 °C (d-f). The inserts in panels a and d show the FIB cross-sections of biotic protodolomites. The degree of cation ordering in the structure can be identified by the FFT patterns (insets in panel c and f).

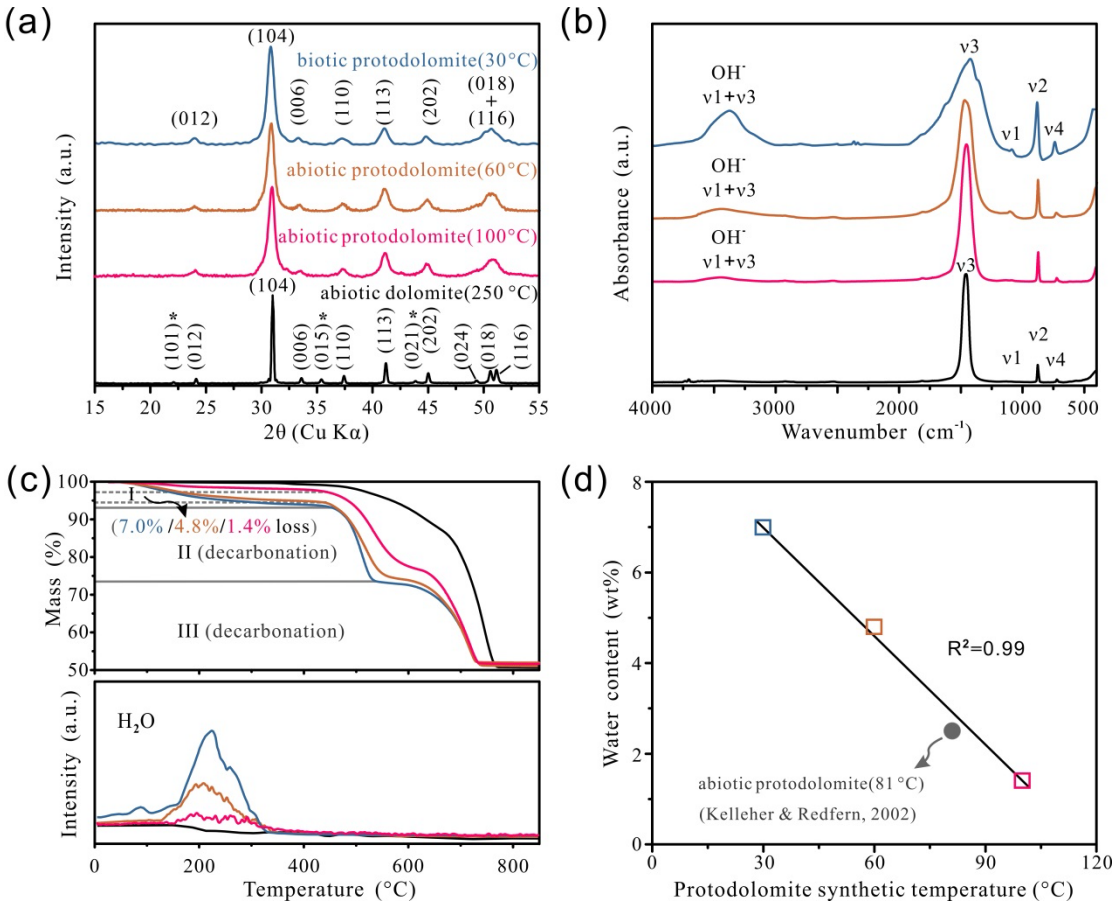
(a)
(104)
biotic protodolomite(30°C)
(012)
(006)
(110)
(113)
(202)
(018)
+
(116)
abiotic protodolomite(60°C)
abiotic protodolomite(100°C)
(104)
abiotic dolomite(250 °C)
(101)*
(012)
(006)
(015)*
(110)
(113)
(021)*
(202)
(024)
(018)
(116)
Intensity (a.u.)
2θ (Cu Kα)
(b)
OH-
v1+v3
v3
v2
v1
v4
Absorbance (a.u.)
Wavenumber (cm-1)
(c)
(7.0% /4.8%/1.4% loss)
II (decarbonation)
III (decarbonation)
Mass (%)
H2O
Intensity (a.u.)
Temperature (°C)
(d)
R²=0.99
abiotic protodolomite(81 °C)
(Kelleher & Redfern, 2002)
Water content (wt%)
Protodolomite synthetic temperature (°C)

Figure 1

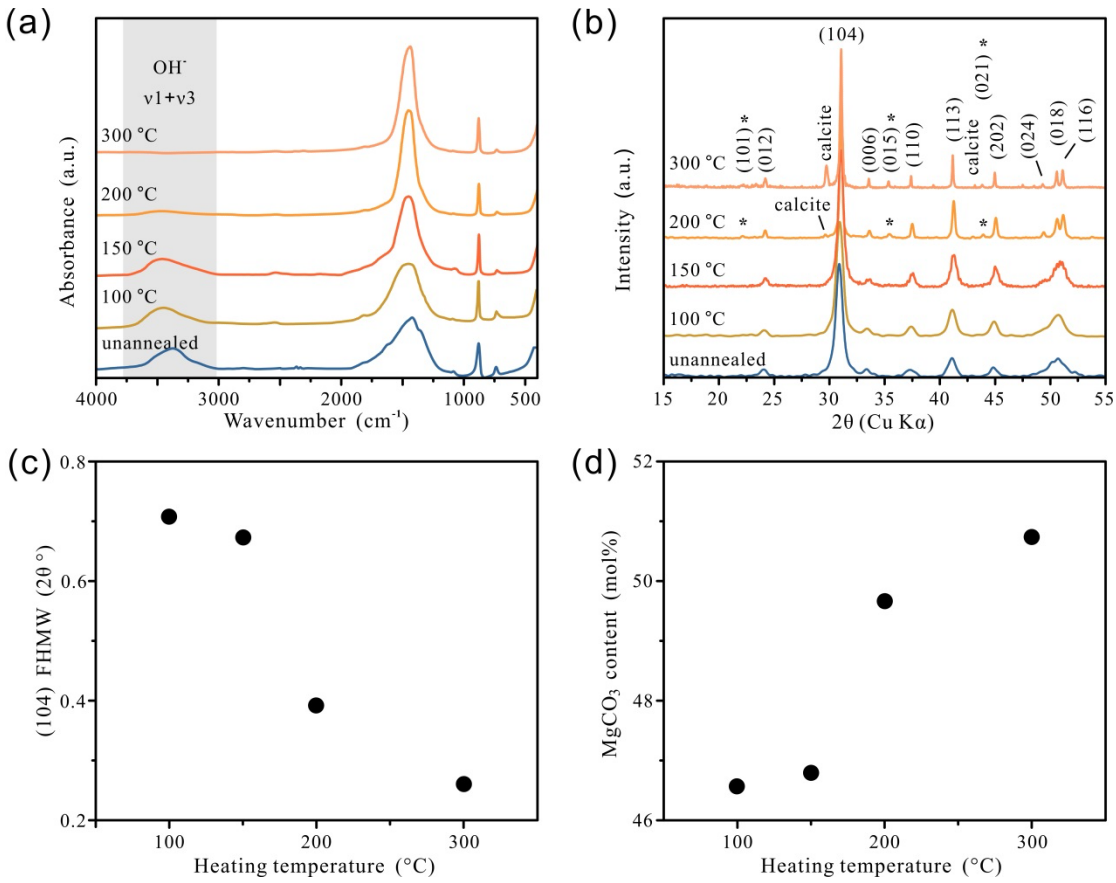
(a)
OH-
ν1+ν3
300 °C
200 °C
150 °C
100 °C
unannealed
Absorbance (a.u.)
4000
3000
2000
1000
500
Wavenumber (cm-1)
(b)
(104)
(101) *
(012)
calcite
(006)
(015) *
(110)
(113)
calcite
(202)
(021) *
(024)
(018)
(116)
300 °C
200 °C
150 °C
100 °C
unannealed
Intensity (a.u.)
15
20
25
30
35
40
45
50
55
2θ (Cu Kα)
(c)
(104) FHMW (2θ °)
0.8
0.6
0.4
0.2
100
200
300
Heating temperature (°C)
(d)
MgCO3 content (mol%)
52
50
48
46
100
200
300
Heating temperature (°C)

Figure 2

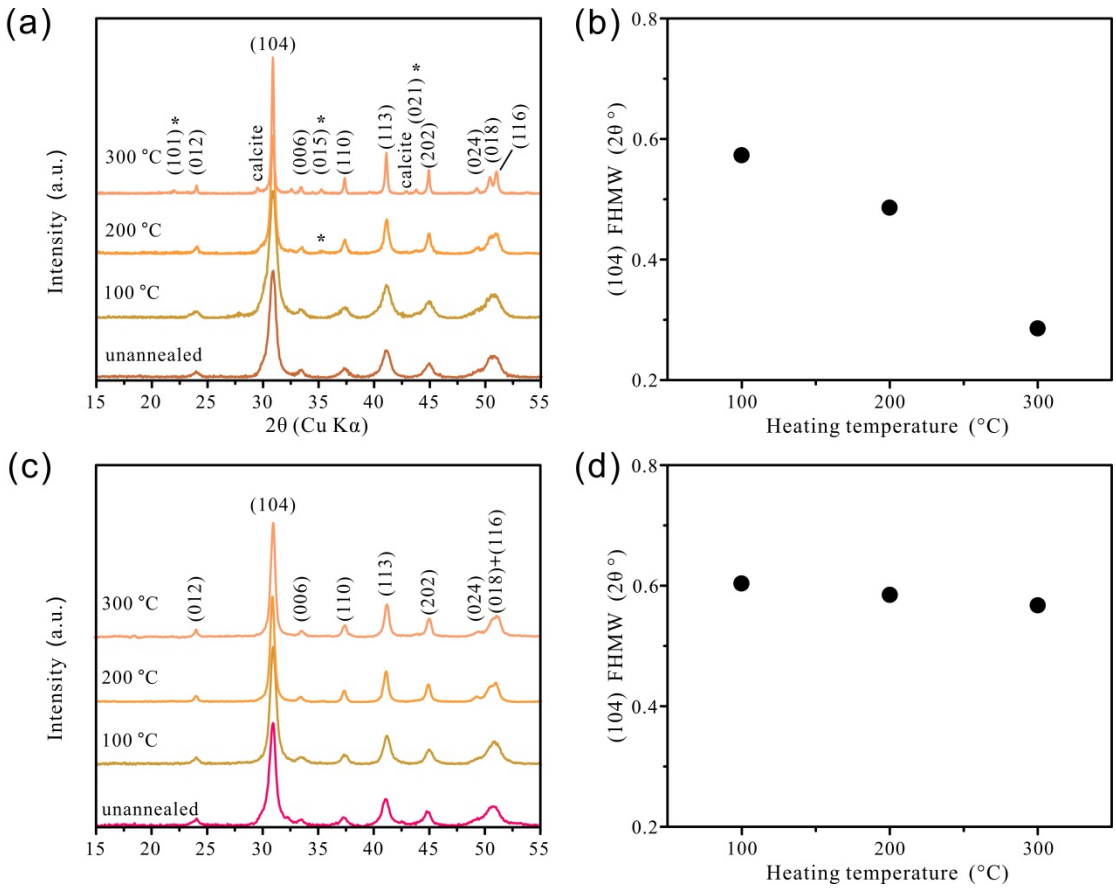
(a)
(104)
(101)*
(012)
calcite
(006)
(015)*
(110)
(113)
calcite
(021)*
(202)
(024)
(018)
(116)
300 °C
200 °C
100 °C
unannealed
*
Intensity (a.u.)
15 20 25 30 35 40 45 50 55
2θ (Cu Kα)
(b)
0.8
0.6
0.4
0.2
(104) FHMW (2θ °)
100 200 300
Heating temperature (°C)
(c)
(104)
(012)
(006)
(110)
(113)
(202)
(024)
(018)+(116)
300 °C
200 °C
100 °C
unannealed
Intensity (a.u.)
15 20 25 30 35 40 45 50 55
(d)
0.8
0.6
0.4
0.2
(104) FHMW (2θ °)
100 200 300
Heating temperature (°C)

Figure 3

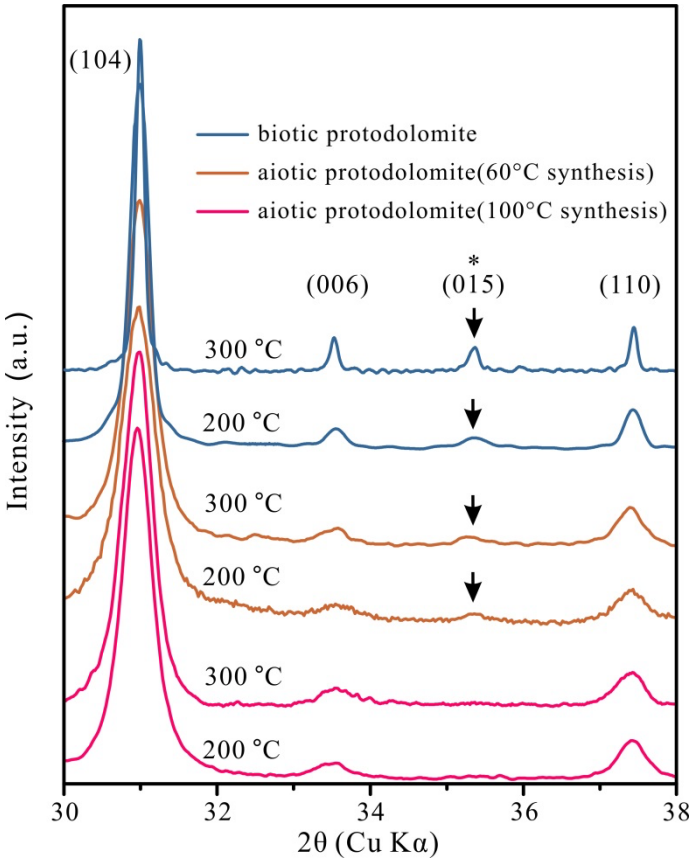
(104)
biotic protodolomite
aiotic protodolomite(60°C synthesis)
aiotic protodolomite(100°C synthesis)
(006)
*
(015)
(110)
300 °C
200 °C
300 °C
200 °C
300 °C
200 °C
Intensity (a.u.)
30
32
34
36
38
2θ (Cu Kα)

Figure 4

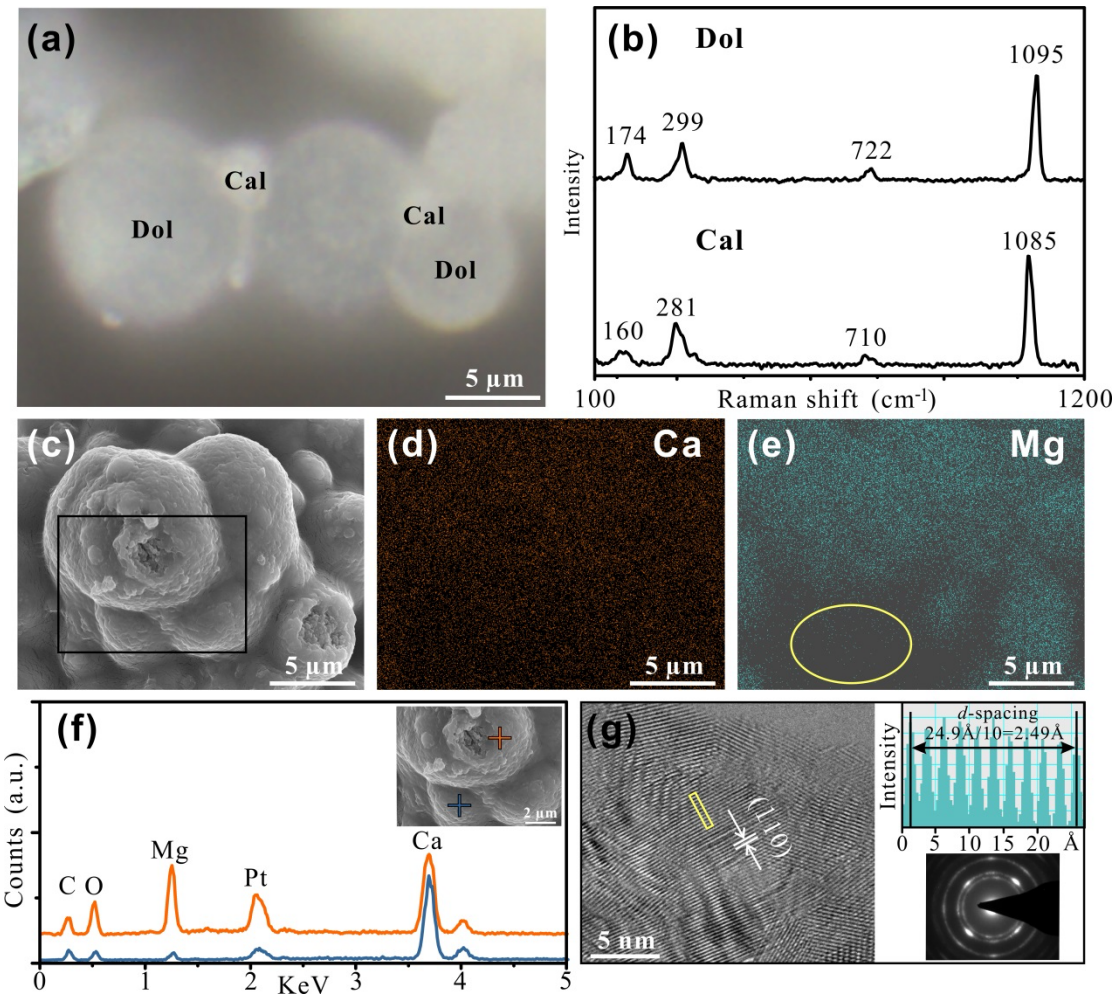
(a)
Cal
Dol
Cal
Dol
5 µm
(b)
Dol
1095
174
299
722
Intensity
Cal
1085
281
160
710
100
Raman shift (cm-1)
1200
(c)
5 µm
(d)
Ca
5 µm
(e)
Mg
5 µm
(f)
2 µm
Counts (a.u.)
C O
Mg
Pt
Ca
0
1
2
KeV
3
4
5
(g)
(110)
5 nm
Intensity
d-spacing
24.9Å/10=2.49Å
0 5 10 15 20 Å

Figure 5

658

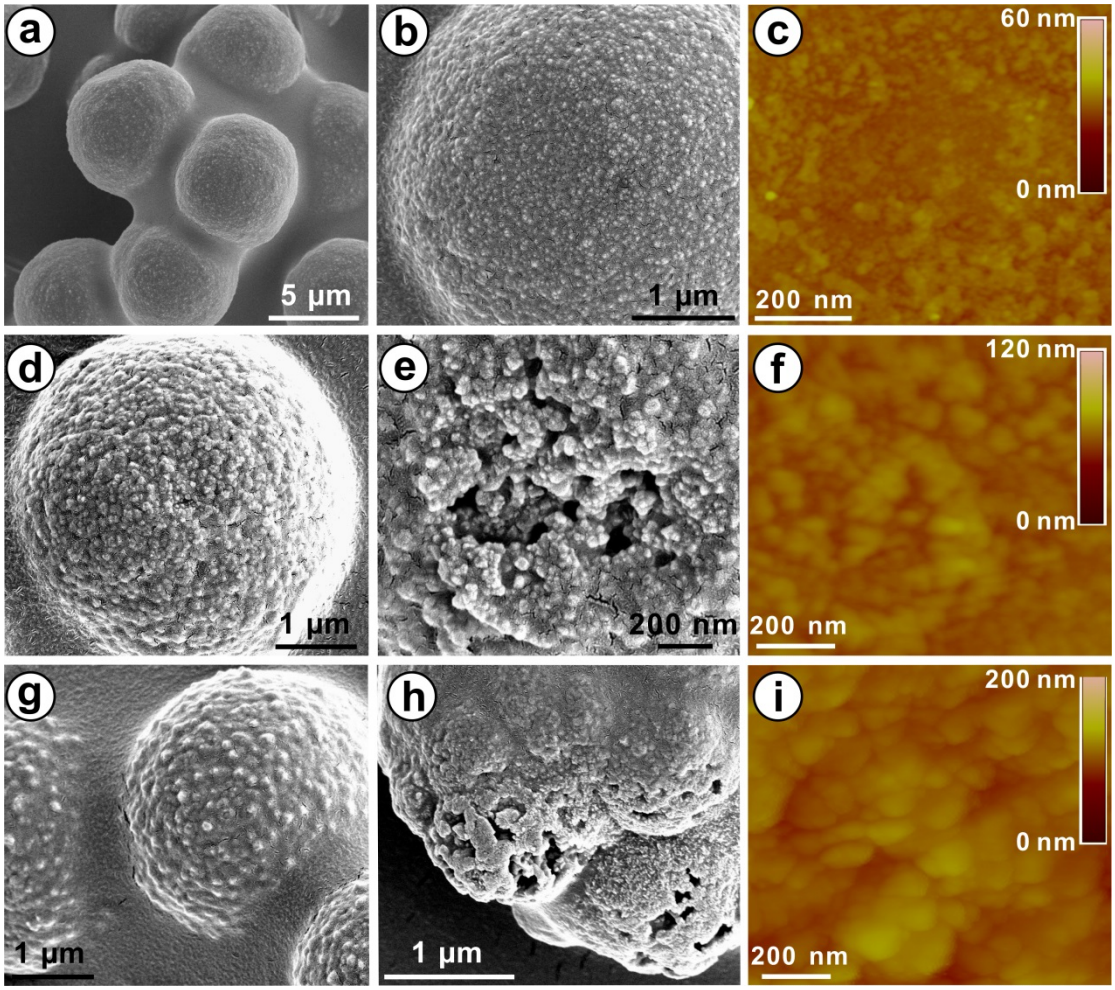
a
5 µm
b
1 µm
c
60 nm
0 nm
200 nm
d
1 µm
e
200 nm
f
120 nm
0 nm
200 nm
g
1 µm
h
1 µm
i
200 nm
0 nm
200 nm

Figure 6

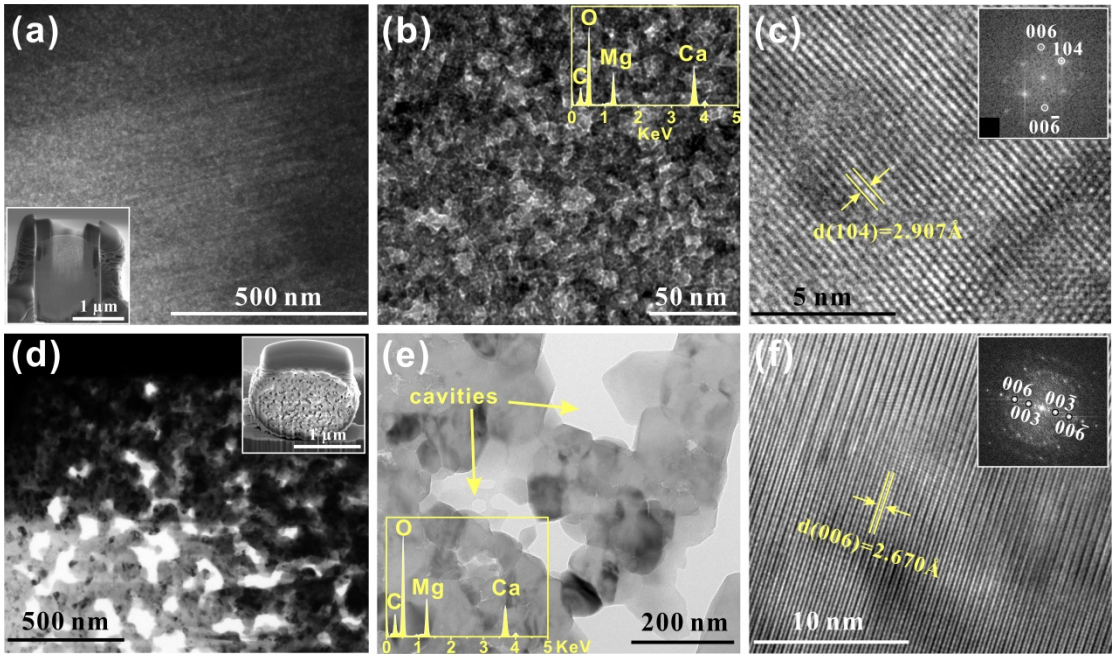
(a)
1 μm
500 nm
(b)
O
Mg
Ca
C
0 1 2 3 4 5
KeV
50 nm
(c)
006
104
00$\bar{6}$
d(104)=2.907 Å
5 nm
(d)
1 μm
500 nm
(e)
cavities
O
Mg
Ca
C
0 1 2 3 4 5 KeV
200 nm
(f)
006
00$\bar{3}$
00$\bar{3}$
00$\bar{6}$
d(006)=2.670 Å
10 nm

Figure 7